

Segmentation and Measurement of the Cortex from 3-D MR Images Using Coupled-Surfaces Propagation

Xiaolan Zeng,* Lawrence H. Staib, Robert T. Schultz, and James S. Duncan

Abstract—The cortex is the outermost thin layer of gray matter in the brain; geometric measurement of the cortex helps in understanding brain anatomy and function. In the quantitative analysis of the cortex from MR images, extracting the structure and obtaining a representation for various measurements are key steps. While manual segmentation is tedious and labor intensive, automatic reliable efficient segmentation and measurement of the cortex remain challenging problems, due to its convoluted nature. Here we present a new approach of coupled-surfaces propagation, using level set methods to address such problems. Our method is motivated by the nearly constant thickness of the cortical mantle and takes this tight coupling as an important constraint. By evolving two embedded surfaces simultaneously, each driven by its own image-derived information while maintaining the coupling, a final representation of the cortical bounding surfaces and an automatic segmentation of the cortex are achieved. Characteristics of the cortex, such as cortical surface area, surface curvature, and cortical thickness, are then evaluated. The level set implementation of surface propagation offers the advantage of easy initialization, computational efficiency, and the ability to capture deep sulcal folds. Results and validation from various experiments on both simulated and real three-dimensional (3-D) MR images are provided.

Index Terms— Coupled-surfaces propagation, level set, 3-D segmentation, volumetric layer.

I. INTRODUCTION

A SIGNIFICANT amount of recent anatomical MRI studies on the human brain have focused on the cerebral cortex. As the outermost layer of gray matter in the brain, the cerebral cortex is composed of columns of neurons aligned perpendicularly to the cortical surface that serve as basic units of information processing. Cortical surface area is likely to be proportional to column number and therefore surface area should be related to functional capacities. In addition, regional cortical thickness and gray-matter volume may relate to functional capacities and alteration in each of these features has been suspected in specific neuropsychiatric disorders [32]. In the quantitative analysis of these features of the cortex, segmentation is the first step.

Manuscript received December 23, 1998; revised July 16, 1999. This work was supported in part by the NIH under Grants NINDS R01 NS35 193-01, NICHD 5 P01 HDIDC 35482, and R01 HL44803, and by the NSF under Grant IRI-9530768. The Associate Editors responsible for coordinating the review of this paper and recommending its publication were M. Viergever and W. Niessen. *Asterisk indicates corresponding author.*

*X. Zeng, L. H. Staib, and J. S. Duncan are with the Departments of Electrical Engineering and Diagnostic Radiology, Yale University, New Haven, CT 06520, USA.

R. T. Schultz is with the Child Study Center, Yale University, New Haven, CT 06520 USA.

Publisher Item Identifier S 0278-0062(99)09103-X.

The cerebral cortex is characterized by its convoluted surface. Due to this convoluted nature, the segmentation of the cortex must be considered in three dimensions. For example, although the cerebral cortical layer is nearly 3 mm thick [1] everywhere on the cortex, an oblique two-dimensional (2-D) slice that happens to be approximately parallel to a particular sulcus will give the appearance of a much thicker structure. Only by going through the neighboring slices can we get complete information to perform segmentation. Slice-by-slice manual tracing of the cortex is extremely tedious and labor intensive, hence, automatic, reliable, and relatively efficient segmentation which enables automated measurement is a highly desirable goal.

A. Related Work

There are a variety of alternatives to our approach. The first group are region-based methods which exploit homogeneity in images. They primarily depend on the underlying consistency of any relevant feature in different regions. Following the work of Geman and Geman [10], Markov random field (MRF)-based methods have been widely used for this purpose, which employ energy-minimizing techniques to reconstruct a piecewise flat image from the noisy data. A multispectral voxel classification method [2] was used in conjunction with connectivity to segment the brain into different tissue types from three-dimensional (3-D) MR images. A material mixture model [19] was also used for the segmentation problem. Region-based methods typically require further processing to group segmented regions into coherent structures. Moreover, quantitative measurement of features other than volume does not follow immediately.

The most common second alternative strategy is boundary finding, of which active contour methods are of special note. They rely mainly on gradient features for segmentation of structures from an image. One of the most generic and popular methods of detecting boundaries is the snakes approach due to Kass *et al.* [13]. One concern regarding this method is that close initialization must be provided in order to achieve good final results. A balloon model with a pressure force outward was then introduced as a way to generalize and solve some of the problems encountered with the above snake method. Deformable surface models using the finite-element method have been used to segment 3-D images [3]. However, the need to override local smoothness to allow for significant protrusions that a shape may possess (which is highly desirable in order to capture the sulcal folds) remains a problem.

An alternative approach to deformable boundary finding was to use a 3-D surface model with Fourier presentation due to Staib and Duncan [35], [36]. The advantage of this model is that it allows a wide variety of smooth surfaces to be described with a small set of parameters. However, it has limitations in capturing convoluted surfaces, such as the cortical surface.

All of the above methods do not explicitly use constraints due to cortical structural information, hence, they are limited for the purpose of cortical segmentation. However, there has been some effort made in this direction. MacDonald *et al.* presented an iterative algorithm for simultaneous deformation of multiple surfaces with intersurface proximity constraints and self-intersection avoidance, where the deformation was formulated as a cost function minimization problem [21], [22]. This method was applied to 3-D MR brain data to extract surface models for the skull and the cortical surfaces. This approach takes advantage of the information of the interrelation between the surfaces of interest. However, drawbacks lie in its extremely high computational expense and the difficulty of tuning the weighting factors in the cost function, due to the complexity of the problem.

Teo *et al.* [38] used a system that exploited knowledge of cortical anatomy, in which white matter and CSF regions were first segmented. After the connectivity of the white matter was verified in regions of interest, a representation of the gray matter was created by a constrained growing out from the white-matter boundary. The focus of this work was to create a representation of cortical gray matter for functional MRI visualization.

Davatzikos *et al.* introduced the concept of a ribbon for modeling the outer cortex in cross-sectional brain images [4] and then extended the model into 3-D [5]. A deformable surface algorithm was constructed to find the central layer of the cortex. Based on this parameterization, the cortical structure was characterized through its depth map and curvature map. This method explicitly used the structural information of the cortex. However, close initialization and significant human interaction are needed to force the ribbon into sulcal folds. To compensate for this, Xu *et al.* further extended the method by using a new external force model, called gradient vector flow, for surface deformation [41].

Dale *et al.* [6] concentrated on cortical surface-based analysis. They started by deforming a tessellated ellipsoidal template into the shape of the inner surface of the skull under the influence of an MRI-based force and a curvature reducing force. White matter was then labeled and the cortical surfaces were reconstructed with validation of topology and geometry.

II. OUR APPROACH

The cortical layer to be recovered has an nearly constant thickness (there is variation across different regions) and is bounded by two surfaces: the CSF/gray-matter boundary and gray-/white-matter boundary. Across each bounding surface there is a local difference in the gray-level values, while in between the two surfaces there is a homogeneity of certain voxel statistics. For our purposes, the cortical layer is defined completely by its bounding surfaces and the homogeneity

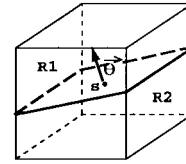


Fig. 1. A local operator to derive image information.

in between. Following our earlier work [42], we propose a new approach of coupled-surfaces propagation via level set methods for the segmentation and measurement of the cortex. By evolving two embedded surfaces simultaneously, each driven by its own image-based information while maintaining the coupling, we are able to achieve an automatic and robust segmentation of the cortex and simultaneously obtain a representation of the inner and outer cortical surfaces from which surface area can be calculated. Furthermore, curvature and thickness maps are easily obtained from this coupled level set formulation.

A. Image Information Derivation

Medical images consist of a number of different anatomical regions. The homogeneity of each region can usually be characterized by various voxel statistics inside. Thus, by using gradient features (information of gray level difference between neighboring voxels) alone, we actually lose important pieces of information. Here in our approach, instead of using gradient features, we design a local operator which makes use of the gray level information, and gives a measure of the likelihood of a voxel lying on the boundary between tissue *A* and tissue *B*. This model can also be extended to make use of a vector of registered parametric images (such as T1, T2, and PD MR images) or images from different modalities.

At each voxel site *s*, a small neighborhood around *s* is drawn (see Fig. 1). Now, given a possible boundary with normal direction $\vec{\theta}$, dividing the neighborhood into parts *R1* and *R2*, the probability that *s* lies on the boundary between tissue *A* and tissue *B* is

$$p_{AB}(\vec{\theta}) = p(R1 \in \text{Tissue } A) \cdot p(R2 \in \text{Tissue } B). \quad (1)$$

Given an estimation $\vec{\theta}^*$ of $\vec{\theta}$, we can use $p(\vec{\theta}^*)$ as a measure of the likelihood that *s* lies on the boundary between tissue *A* and tissue *B*.

One way of estimating $\vec{\theta}^*$ is to first generate the vector $P = [p(\vec{\theta}_1), p(\vec{\theta}_2), \dots, p(\vec{\theta}_k)]^T$ where *k* is the number of possible directions corresponding to the 26 first-order neighbors. Then, $\vec{\theta}^*$ is the direction which corresponds to the element in vector *P* that has the largest magnitude. Here we make the assumption of one single parametric image *X*, in which voxels belonging to tissue *A* are independently drawn from a Gaussian distribution $G(\mu_A, \sigma_A)$ and voxels belonging to tissue *B* are independently drawn from $G(\mu_B, \sigma_B)$. Thus, we have

$$p_{AB}(\vec{\theta}) = \prod_{r \in R1} \frac{1}{\sqrt{2\pi}\sigma_A} e^{-((X_r - \mu_A)^2 / \sigma_A^2)} \cdot \prod_{t \in R2} \frac{1}{\sqrt{2\pi}\sigma_B} e^{-((X_t - \mu_B)^2 / \sigma_B^2)}. \quad (2)$$

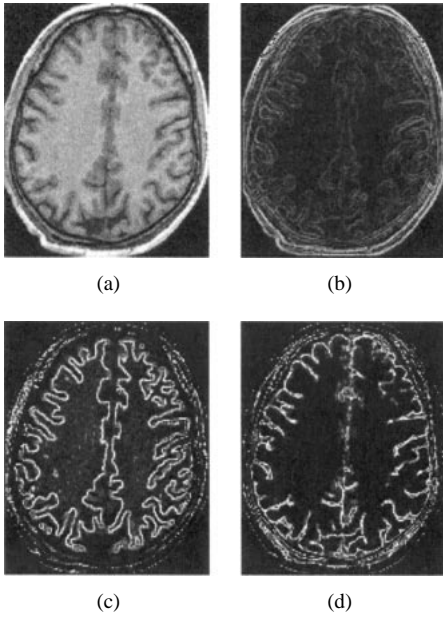


Fig. 2. Results from our local operator compared to image gradient. (a) An axial slice from original 3-D brain images. (b) Result from gradient operator. (c) Result from our local operator $p_{BC}(\tilde{\theta}^*)$, B = gray matter, C = white matter. (d) $p_{AB}(\tilde{\theta}^*)$, A = CSF, B = gray matter.

In our implementation, $R1$ and $R2$ are now set to include one voxel each. A limited expansion to several voxels could potentially further enhance the capability of capturing homogeneity. In Fig. 2, we show an example of the results from our local operator, showing how well it selects the appropriate gray-level transition which is crucial for subsequent processing. The local operator was applied to images after we reduced the effects of MR inhomogeneity by correcting, using a simple fixed map. The map was determined manually by sampling tissue types throughout the field to decide the average inhomogeneity. Note that more complicated MR image models [10], [17], [18] can be used to calculate $p(\tilde{\theta})$.

B. Level Set Method

Level set methods are powerful numerical techniques for analyzing and computing interface motion, and have been used in image segmentation in recent years [23]–[25], [33], [34]. The essential idea of the level set methods is to represent the propagating surface (in our case) of interest as a front $\gamma(t)$ and embed this front as the zero level set of a higher dimensional function Ψ defined by $\Psi(x, t) = d$, where d is the signed distance from position x to $\gamma(t)$. A Eulerian formulation is produced for the motion of this surface, propagating along its normal direction with speed F where F can be a function of the surface characteristics (such as the curvature, normal direction, etc.) and the image characteristics (e.g., gray level and gradient, etc.). The equation of the evolution of Ψ , inside which the propagating surface is embedded as the zero level set, is then given by

$$\Psi_t + F|\nabla\Psi| = 0. \quad (3)$$

The major advantages of using this method over other active contour strategies include the following. First, although

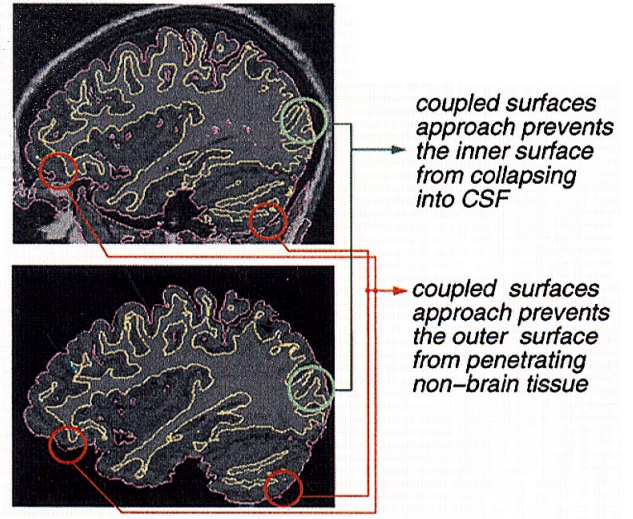


Fig. 3. Single-surface versus coupled-surfaces approach on cortex segmentation. Top: surfaces resulting from single-surface approach shown on a sagittal slice of original image (finding the inner and outer cortical surfaces separately); bottom: surfaces resulting from the coupled-surfaces approach shown on a sagittal slice of the expert tracing result. Notice that the outer cortical surface resulted from the coupled 3-D algorithm nicely fits the boundary from expert tracing.

the evolving level function $\Psi(x, t)$ remains a function, the embedded propagating front $\gamma(t)$ may change topology, break, merge, and form sharp corners as Ψ evolves. Second, the intrinsic geometric properties of the front may be easily determined from Ψ . For example, at any point of the front, the normal vector is given by $\vec{n} = \nabla\Psi$.

C. Single-Surface Approach Versus Coupled-Surfaces Approach

Because of the limitations of the imaging technique used and the volume averaging effect, it is often observed that in some regions there is not enough information from the image data to clearly define either the outer or the inner bounding surface. When applying a single-surface approach, we may very well end up with error in such a region. While using the coupled-surfaces approach, information on the partner surface is available through the coupling and improves the performance of the surface finding.

In the case of MR brain images, due to volume averaging, in some regions, the boundary between white matter and gray matter is not well shown, while the CSF appears clearly. The single-surface approach may hence have the inner cortical surface collapse into CSF. However, with the coupled-surfaces approach, we maintain some minimal distance between the inner cortical surface and CSF, thus preventing the inner cortical surface from going into CSF. There are also places where structures such as eye sockets appear, so that the CSF cannot be observed in the image. With the coupled-surfaces approach, the white-/gray-matter boundary information is then used to stop the propagation of the outer cortical surface before it penetrates nonbrain structures. Fig. 3 shows examples of the above-mentioned cases where the coupled-surfaces approach outperforms the single-surface approach.

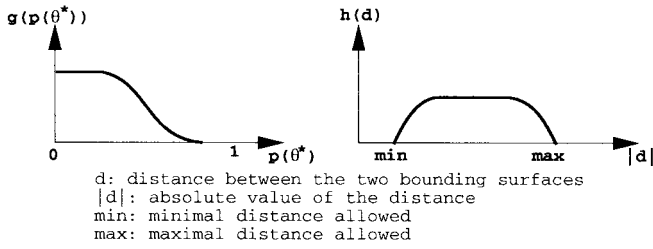


Fig. 4. Functions g and h used in speed term design.

D. Coupled-Surfaces Propagation: Speed Term Design

In solving the problem of segmenting the cortex, we consider two moving interfaces describing the inner and outer cortical bounding surfaces, respectively. Starting from inside the inner cortical surface (i.e., inside the white matter) with an offset in between (see Fig. 7), the interfaces propagate along the outward normal direction, stopping at the desired place, while maintaining a certain distance between them.

Embedding each surface as the zero-level set in its own level function, we have two equations

$$\Psi_{\text{in}_t} + F_{\text{in}}|\nabla\Psi_{\text{in}}| = 0 \quad (4)$$

$$\Psi_{\text{out}_t} + F_{\text{out}}|\nabla\Psi_{\text{out}}| = 0 \quad (5)$$

where F_{in} and F_{out} are functions of the surface normal direction, image-derived information, and distance between the two surfaces. The coupling is embedded in the design of F_{in} and F_{out} . At places where the distance between the two surfaces is within a normal range, the two surfaces propagate according to the image-based information. Where the distance between the two surfaces is out of the normal range, the distance imposes a constraint on the propagation of the surfaces.

With the level set implementation we have a natural way to establish a correspondence between the points on the two evolving surfaces through distance, which is evaluated with little extra computational expense. Recall that the value of the level function of a front at any point is simply the distance from this point to the current front which, as in [33], is calculated as the shortest distance from this point to all the points on the front. In our case of two moving surfaces, for any point on the inner moving surface, the distance to the outer moving surface is the value Ψ_{out} at this point and vice versa for the point on the outer moving surface. Hence, we write

$$F_{\text{in}} = g(p_{BC}(\vec{\theta}^*))h(\Psi_{\text{out}}) \quad (6)$$

$$F_{\text{out}} = g(p_{AB}(\vec{\theta}^*))h(\Psi_{\text{in}}) \quad (7)$$

where g and h are the functions, as shown in Fig. 4, and A, B, C denote CSF, gray matter, and white matter respectively.

Function g maps larger likelihood to slower speed, i.e., as the likelihood gets larger, g tends to zero, while as the likelihood gets to near zero, g tends to a constant. Function h penalizes the distance off the normal range. As the distance goes out of normal range, h goes to zero. Thus, each surface moves with constant speed along its normal direction and slows down when either the image-based information becomes

strong or the distance to the other surface moves away from the normal range. Each surface finally stops when the image-derived information is strong enough or the distance to the other surface is out of the normal range.

Based on the fact that the speed terms are designed to force the propagating level set to stop at the desired boundary, the image-dependent speed terms have meaning only on the front, i.e., the zero level set. However, the level set equation of motion is written for the function Ψ , defined over the entire image grid. We thus extend the speed terms from the zero level set to the whole image grid, as in [33], i.e., point b takes on the speed of point a , which is the closest point to b and lies on the zero level set.

Due to the level set formulation, we have a notion of the inside and outside of the current moving front, which is embedded in the outward normal direction \vec{n} . This information can be used to reduce the feasible space of possible $\vec{\theta}$ s, or \vec{n} can be used directly as an estimate of $\vec{\theta}^*$, thus obtaining a better result.

E. Narrow-Band Method and Distance Correspondence

For computational efficiency, the algorithm is implemented using a narrow-band method [33], which modifies the level set method so that it only explicitly updates the points close to the current propagating fronts. Our implementation of the narrow-band method uses this idea, but is designed specifically for coupled level sets so that the distance between the two embedded surfaces (necessary for the computation of the speed terms) is available with no further computation after narrow-band rebuilding.

Based on the fact that any point b in the narrow band of the current surface should be within some neighborhood of a certain point a on the current surface, the narrow band is constructed dynamically in the 3-D neighborhood of each point on the current surface by including points that lie within a certain distance range (i.e., bandwidth) away from that particular point. Also, since a point b in the narrow band can be within the neighborhood of several points a_1, \dots, a_l on the current surface, we update the value of the level function Ψ at b to be

$$\text{sign}(\Psi(b)) \cdot \left(\min_{i=1, \dots, l} \text{dist}(b, a_i) \right)$$

where function dist gives the positive Euclidean distance.

The steps for rebuilding the narrow band and updating Ψ inside the band are as follows:

```

for every point  $a$  on the current front {
  for every point  $b$  in the neighborhood of  $a$  {
    if  $b$  is not already in the narrow band,
      then add  $b$  to the narrow band;
    if  $\text{dist}(b, a)$  is less than
      the absolute value of the current  $\Psi(b)$ ,
      then update  $\Psi(b)$  to be  $\text{sign}(\Psi(b)) \cdot \text{dist}(b, a)$ ;
  }
}
```

The size of the neighborhood depends on the allowed bandwidth and therefore is fixed. Thus, for a surface represented

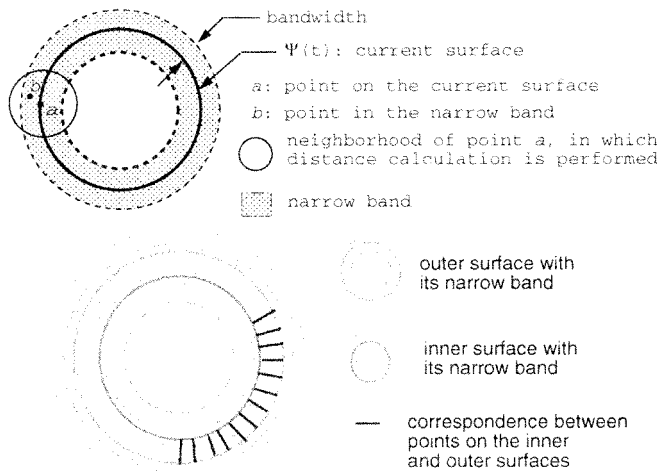


Fig. 5. Schematic of narrow-band implementation for 2-D curve case (same argument holds in 3-D). Top: dynamic construction of the narrow band and the update of the level function Ψ within are performed in the neighborhood of the current surface. Bottom: inner and outer surfaces with their narrow bands. Notice the inner surface lies within the narrow band of the outer surface, and vice versa.

Algorithm Diagram

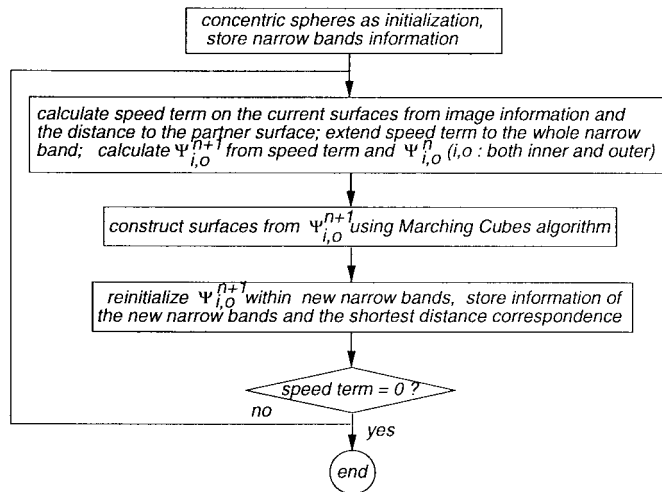


Fig. 6. Algorithm diagram.

using N points, the construction of its narrow band and the update of Ψ in the narrow band is an $O(N)$ calculation.

In our application, two different narrow bands are computed for the inner and outer interfaces, respectively. As shown in Fig. 5, to ensure that the distance-based correspondence between the coupled surfaces falls out automatically, the two bandwidth ranges (for the inner and outer narrow bands separately) are chosen such that the inner surface lies within the narrow band of the outer surface and vice versa. Thus, at each time step, the current position of the propagating coupled surfaces and the surrounding narrow bands are estimated and the whole process repeats until the speed terms for both the inner and outer surfaces reach a zero value everywhere. To summarize, the algorithm diagram is shown in Fig. 6.

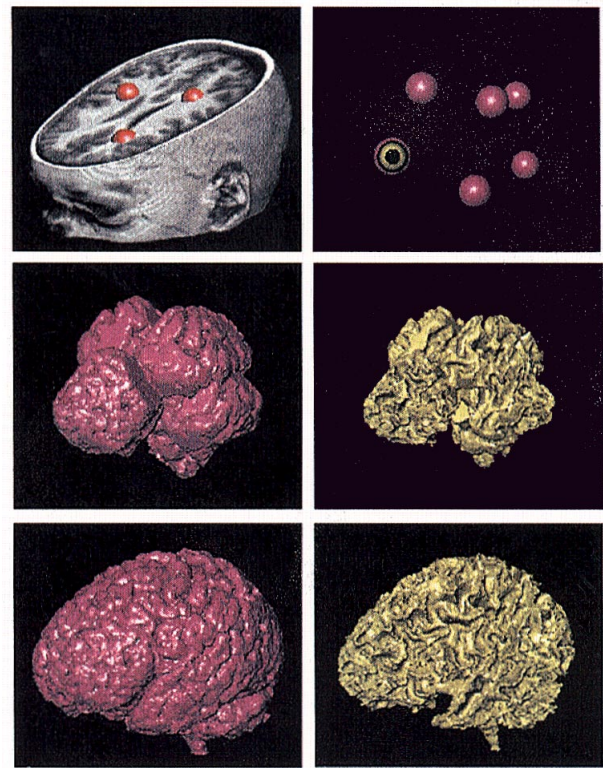


Fig. 7. Propagation of the outer (pink) and inner (yellow) bounding surfaces. Top: pairs of concentric spheres (only the outer ones are shown on the left, both are shown with a cutting plane on the right) as initialization in unedited 3-D MR brain images; middle: intermediate step in surface propagation; bottom: final result of the outer and inner cortical surfaces.

F. Measurement

With the coupled-surfaces propagation via level set methods, it is easy to perform various measurements on the cortical layer with little extra computational expense. Whole brain volume, cortical gray-matter volume, white-matter volume, cortical surface area, cortical surface shape, and cortical thickness maps are among the features most interesting in the study of brain structure and function. Different combinations of the above measurements may help in determining the pathobiology of various neuropsychiatric disorders. We now discuss one by one the above measurements from our coupled-surfaces formulation.

Volume: With the signed distance function Ψ , the level set formulation keeps track of the inside and outside of the current moving front. Once the evolution of the coupled surfaces is completed, the cortical gray-matter voxels are those that lie inside the outer cortical surface while outside the inner cortical surface. In the same fashion, nonbrain tissue voxels will be the ones that are outside the outer cortical surface and voxels of white matter will lie inside the inner cortical surface, except for subcortical gray matter and ventricles.

Because the signed-distance-based measures have a sub-voxel accuracy, we can obtain a subvoxel segmentation instead of a binary segmentation on the data set. In other words, if the distance from a voxel to the zero level set surface is less than the voxel size in width, the voxel is considered to contain multiple tissue types.

Surface Area: A marching cubes algorithm [20] is performed on the signed distance functions, Ψ_{in} and Ψ_{out} to extract the embedded zero level sets. The resulting surfaces are realized using a triangular representation. Surface area is then calculated as the sum of the areas of the triangles.

Surface Curvature and Shape Index: As discussed above, one advantage of the level set implementation is that geometric properties of the propagation front are easily calculated [33]. In our case of surfaces propagating in 3-D space, there are many choices for the curvature of the front (for formal definitions of the curvatures, refer to [7]), including mean curvature κ_M and Gaussian curvature κ_G . Both may be conveniently expressed [33] in terms of the level set function Ψ

$$\kappa_M = \frac{\sum_{(i,j,k) \in C} ((\Psi_{ii} + \Psi_{jj})\Psi_k^2 - 2\Psi_i\Psi_j\Psi_{ij})}{2(\Psi_x^2 + \Psi_y^2 + \Psi_z^2)^{3/2}} \quad (8)$$

$$\kappa_G = \frac{\sum_{(i,j,k) \in C} (\Psi_i^2(\Psi_{jj}\Psi_{kk} - \Psi_{jk}^2) + 2\Psi_i\Psi_j(\Psi_{ik}\Psi_{jk} - \Psi_{ij}\Psi_{kk}))}{(\Psi_x^2 + \Psi_y^2 + \Psi_z^2)^2} \quad (9)$$

where $C = \{(x, y, z), (y, z, x), (z, x, y)\}$ is the set of circular shifts of (x, y, z) .

The maximum principle curvature κ_1 and the minimum principle curvature κ_2 are related to Gaussian and mean curvatures through the following formulas:

$$\kappa_1 = \kappa_M + \sqrt{\kappa_M^2 - \kappa_G}, \quad \kappa_2 = \kappa_M - \sqrt{\kappa_M^2 - \kappa_G}.$$

We also adopt the classification of surfaces by Koenderink [15], using the numerical relationship between the two principal curvatures. A shape index function is defined as $si = (2/\pi) \arctan((\kappa_1 + \kappa_2)/(\kappa_1 - \kappa_2))$, which classifies the surfaces into nine types, as show in Fig. 11. With the shape index, gyri (mostly ridges) and sulci (mostly ruts) are automatically identified. Further potential use of the shape index includes the definition of an atrophy index (sulci widen with age).

Thickness Map: As discussed above, the value of the level function of a front at any point is the distance from this point to the current front. Also recall that the inner and outer surfaces are the zero level sets of Ψ_{in} and Ψ_{out} . Thus, for any point on the outer surface, the absolute value of Ψ_{in} at the point is simply the distance from the point to the inner surface. Using this measure, we obtain a thickness map between the inner and outer cortical surfaces which can be used to study the normal thickness variations across different regions of the brain and also the abnormalities in brain structures.

III. EXPERIMENTAL RESULTS

In this section, we show validations of our approach on various simulated and real MR data, as well as applications to specific cortical studies. We use only T1-weighted images because they provide the best gray/white contrast [31] and are therefore commonly used for neuroanatomical analysis.

A. Validation on Simulated MR Data with Ground Truth

We first present our segmentation results using the simulated MR brain images provided by the McConnell Brain Imaging Center at the Montreal Neurological Institute [12]. The images are generated using an MRI simulator [16] which allows users to independently control various acquisition parameters to obtain realistic MR images. The ground truth of the phantom is provided in the form of membership functions of each voxel belonging to different tissue types, such as the skull, CSF, gray matter, and white matter.

The simulated data we tested our algorithm on were T1 images of a normal brain, with the following parameter settings: voxel size = 1 mm³, noise = 3%, and intensity nonuniformity = 0%. Starting from the unedited images, no further user interaction is needed after specifying several pairs of concentric spheres as initialization. The spheres grow out and automatically lock onto the inner and outer cortical surfaces. As long as the spheres are placed inside the white matter, the algorithm is robust to the starting position. Measurement of the volume is then done as described in the previous section. We use a binary segmentation in this experiment. In our implementation of cortex segmentation, the allowed distance between the inner and outer surfaces is set to range from 1.5 to 5.5 mm, based on knowledge from reported postmortem studies [1]. Therefore, to ensure the proper overlapping of the inner and outer narrow bands, the bandwidth ranges for the inner and outer interfaces are chosen to be (−3 mm, 6 mm) and (−6 mm, 3 mm), respectively.

To evaluate the segmentation result, we apply several measures defined as follows. For any tissue type T in the region of interest, we denote the voxels of tissue type T recovered from our 3-D algorithm as V_a and the voxels that are mostly of tissue type T according to the phantom (i.e., the value of tissue T membership function is greater than 0.5) as V_e . We denote the overlap of V_a and V_e as V_{ae} and the part that is in V_a but not in V_e as $V_{ae'}$. A true positive (TP) rate is then defined to be the size of V_{ae} relative to the size of V_e , while the false positive (FP) rate is defined to be the ratio of the size of $V_{ae'}$ to the size of V_e . We also define the volume ratio to be the volume of all the voxels segmented as of tissue type T by our algorithm to the total subvoxel volume of tissue type T , specified by the phantom (subvoxels contribute in only part of the voxel volume).

Table I shows our measurement results over 3 types: total brain tissue (including white matter and gray matter); cortical gray matter in selected slices; and white matter. Since the algorithm is designed specifically for the nearly constant thickness of the cerebral cortex, it recovers only part of the gray matter in the brain stem and the cerebellum where the constant thickness constraint is not well satisfied. These regions account for most of the errors in the TP rate and volume ratio for whole brain tissue. For the same reason that the algorithm is specifically tailored for the cerebral cortex, we would compare the cortical gray-matter volume only in the cerebrum. Since the phantom data does not provide the information related to partitioning the cerebrum, the cerebellum, and the brain stem, we only compare the

TABLE I

COMPARISON OF OUR VOLUME MEASUREMENTS WITH THE PHANTOM GROUND TRUTH. WHOLE BRAIN: TOTAL BRAIN TISSUE (WHITE+GRAY MATTER); CORTICAL GRAY MATTER *: CORTICAL GRAY MATTER ON THE FRONTAL 49 CORONAL SLICES AND THE TOP 56 AXIAL SLICES

%	whole brain	cortical gray matter *	white matter
TP rate	92.3	92.8	92.4
FP rate	2.0	6.0	3.3
volume ratio	96.3	103.2	98.1

cortical gray-matter volume on selected slices where the cerebellum and brain stem are excluded: frontal, 49 coronal slices and top, 56 axial slices. The resulting average error of the TP and FP rate is around 6–7%, and the volume ratio error is within 4%. For the white matter, the errors for the TP, FP rate, and volume ratio are also low. These results show that our algorithm performs well in isolating the brain from nonbrain tissues and in segmenting the cortex.

B. Validation on 20 Normal Brains

To further evaluate our segmentation approach under a wide range of imaging conditions, we tested the algorithm on real MR data and compared the results obtained with gray segmentation by manual experts. Since for 3-D data it is a very labor intensive job to segment gray and white matter, we utilized the data provided by the Internet Brain Segmentation Repository (IBSR) of the Center for Morphometric Analysis (CMA) at Massachusetts General Hospital [11].

The purpose of IBSR is to encourage the development and evaluation of segmentation methods by providing test image data, human expert segmentation results, and methods for comparing segmentation results. It is one of the first efforts to offer solutions to the problem of validating and comparing new algorithms in this rapidly growing medical image analysis field. The test image data sets provided in this repository permit a standardized mechanism for evaluation of the sensitivity of a given analysis method to signal to noise ratio, contrast to noise ratio, shape complexity, degree of partial volume effect, etc.

We obtained 20 normal MR brain data sets and their manual segmentations from IBSR. These 20 coronal 3-D T1-weighted spoiled gradient echo MRI scans were performed on two different imaging systems. Ten FLASH scans on four males and six females were performed on a 1.5-T Siemens Magnetom MR System (Iselin, NJ) with the following parameters: TR = 40 ms, TE = 8 ms, flip angle = 50°, field of view = 30 cm, slice thickness = contiguous 3.1 mm, matrix = 256 × 256, and averages = 1. Ten 3-D-CAPRY scans on six males and four females were performed on a 1.5-T General Electric Signa MR System (Milwaukee, WI), with the following parameters: TR = 50 ms, TE = 9 ms, flip angle = 50°, field of view = 24 cm, slice thickness = contiguous 3.0 mm, matrix = 256 × 256, and averages = 1.

All data sets were positionally normalized at CMA by imposing a standard 3-D brain coordinate system on each 3-D MR scan, using the midpoints of the decussations of the

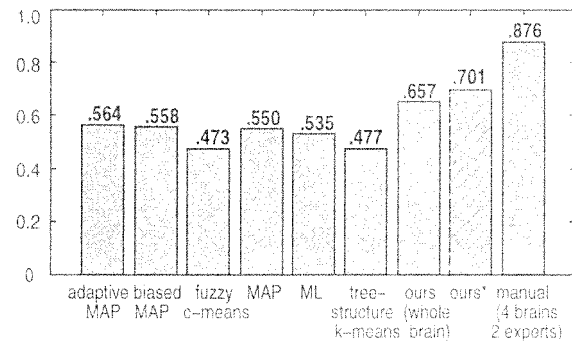


Fig. 8. Average overlap metric for gray-matter segmentation on 20 normal brains from various segmentation methods. The results of automatic segmentation methods provided by IBSR were from work done by Rajapakse. MAP: maximum *a posteriori* probability. ML: maximum likelihood. *: using frontal 13 coronal slices and upper 50 axial slices of each brain to exclude brain stem and cerebellum.

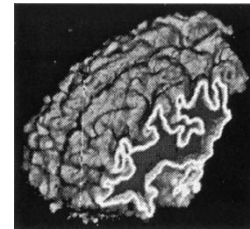


Fig. 9. Three-dimensional volume rendering of the frontal lobe cortex with an oblique cutting plane. The convoluted thin bright ribbon is the cortical gray matter captured on the cutting plane.

anterior and posterior commissures and the midsagittal plane at the level of the posterior commissure as points of reference for rotation and (nondeformation) transformation [37], [8]. The repositioned scans were then resliced into normalized 3.0-mm coronal, 1.0-mm axial, and 1.0-mm sagittal scans which were used for subsequent analysis.

Manual segmentation was performed on the normalized scans by trained investigators at CMA using a semiautomated intensity contour mapping algorithm [14], [11]. Once the external border was determined by intensity contour mapping, grey-white-matter borders were demarcated, using signal intensity histograms. Using this technique, borders were defined as the midpoint between the peaks of the bimodal histogram for a given structure and its adjacent tissue. Other neuroanatomical structures were segmented similarly [9].

An overlap metric is used by IBSR to compare results from automatic segmentation and manual segmentation. While manual segmentations are not ground truth, they provide a reasonable way to compare automated segmentation methods. The overlap metric is defined for a given voxel class assignment as the number of voxels that have the class assignment in both segmentations, divided by the number of voxels where either segmentation has the class assignment, which is equivalent to $TP/(1 + FP)$. This metric ranges from 1.0 for perfect agreement, to 0.0 for no agreement of classified voxels.

We interpolated the image data into 1-mm-thick coronal slices and then ran our coupled-surfaces algorithm. Fig. 8 shows the overlap metric for gray-matter segmentation on 20 normal brains from the manual method, various automatic

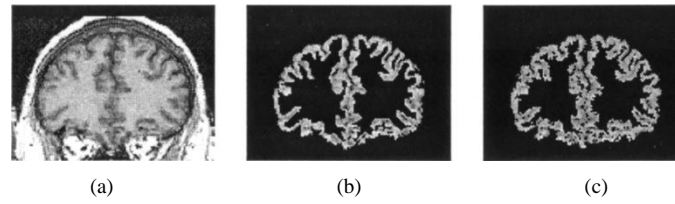


Fig. 10. Coronal slices from 3-D images. (a) Original image. (b) Cortical gray matter from manual tracing. (c) Cortical gray matter from our 3-D algorithm.

segmentation methods and our coupled-surfaces algorithm. The results from the automatic segmentation provided by IBSR were from work done by Rajapakse and partially based on the methods described in [26]. The gray-matter overlap metric for our algorithm on the whole brain is 0.657, which is well above those from the other six listed automatic methods ranging from 0.473 to 0.564 (shown in columns one to six in Fig. 8). Since our algorithm is designed specifically for the cerebral cortex, we compute an improved overlap metric on the upper and frontal part of the brain (to exclude brain stem and cerebellum) of 0.701. Moreover, considering that the other six listed automatic methods started with brain-only data sets, while the coupled-surfaces algorithm started with unstripped brain images, the advantage of our method with geometric structural constraints is clear.

These 20 brain scans were chosen by IBSR because they have been used in published studies [26] and cover a range of image quality [11], with the worst ones having low contrast and relatively large intensity inhomogeneities. The overlap scores shown in Fig. 8 from the automatic classification methods may appear low, however, they need to be taken into the context of a wide range of image quality, and should not be compared with numbers from different studies. More recently acquired (i.e., better quality) data should result in far better results from the automatic classification methods, which holds for our coupled-surfaces algorithm as well. In fact, as shown in the section above, the overlap metric for our phantom cortical segmentation is $0.928/(1 + 0.060) = 0.875$, which compares well with the manual overlap metric of 0.876 showing interoperator reproducibility from tests on four brains averaged over two experts (see Fig. 8). With the rapid growth of medical image processing, it is virtually impossible to implement all the novel methods published and compare results. However we take this study as our initial step toward more extensive evaluation of our algorithm with the help of IBSR, and we intend to carry out more studies.

C. Results on Real MR Data for Frontal Lobe Study

We then tested our algorithm on frontal lobes of seven high-resolution MRI data sets (SPGR, 2NEX, $1.2 \times 1.2 \times 1.2 \text{ mm}^3$ voxels) from a randomly chosen subset of young adult autistic and control subjects from our ongoing studies to measure frontal lobe volume. After preprocessing to reduce the effects of MR bias field inhomogeneity using a simple standard nonlinear map (this is also a step before expert manual tracing), we ran the coupled-surfaces algorithm to isolate the brain tissue and segment the cortex (see Fig. 7). The frontal lobe was then manually defined independently in the left and right hemispheres as all tissue anterior to the central

TABLE II
OUR MEASUREMENTS COMPARED WITH EXPERT
TRACING RESULTS ON SEVEN FRONTAL LOBES

frontal lobe		frontal lobe cortex	
TP(%)	FP(%)	TP(%)	FP(%)
93.8	3.4	83.6	25.5
93.9	1.9	86.2	20.1
95.2	2.9	86.5	24.4
93.7	1.7	86.7	24.5
94.5	1.5	88.9	21.2
94.1	1.7	87.0	20.5
94.1	1.4	89.0	19.5

sulcus, excluding subcortical nuclei [28]. We then create a mask of the frontal lobe and use it to exclude the posterior part of the volume.

Fig. 9 shows a 3-D volume rendering of the cortical gray matter of a frontal lobe, resulting from our algorithm. In Fig. 10, 2-D coronal slices of the same result are shown. As shown in Table II, over the seven frontal lobes, the TP and FP rate (compared to manual tracing by our neuroanatomy specialist) of the whole frontal lobe averaged 94.1% and 2.1%, respectively, which demonstrated that our algorithm nicely isolated the brain tissue from the nonbrain tissue. The average TP and FP rate for the cortical gray matter (measured on two orthogonal slices, one coronal and one axial, over the entire range of the frontal lobe) in the frontal lobe were 86.7% and 20.8%. As we see in Fig. 10, the expert tracing tended to be more aggressive in defining the gray/white-matter boundary, which resulted in the relatively larger value of the FP rate. Note that the FP rate on gray/white segmentation is a very sensitive measure, especially considering the fact that manually drawing a boundary between gray and white matter to some extent depends on subjective individual judgment. However, in quantifying the difference between populations, despite the FP rates, the volume measurements would still yield useful information as long as they are consistent.

The volume of the constituent parts of the brain is typically the measurement of interest for comparison among different subjects in studies of neuroanatomy. Thus, as a second way to analyze the utility of our algorithm, we compute reliability statistics on the volume measurements using the methods described in [31] (see also [42]). There was strong agreement between the algorithm and the expert on the volume of the frontal lobe (Pearson $r = .991$; intraclass correlation coefficient [ICC] = .901). The algorithm systematically estimated the frontal lobe volume to be less than the expert tracer (mean

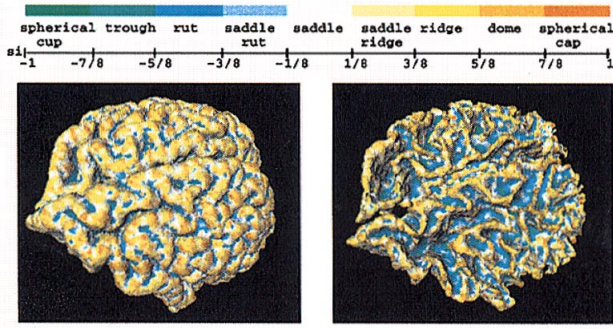


Fig. 11. The outer and inner cortical surfaces of a frontal lobe colored with the specified spectrum representing shape index si .

difference = 4%) and this accounts for the lower ICC than the Pearson coefficient. Similarly, for gray-matter volume of the frontal lobe there was also good agreement (Pearson $r = .96$). Thus, for both whole frontal lobe volume and frontal gray-matter volume, the coupled-surfaces algorithm produced measurements that were very similar to expert tracings.

Fig. 11 shows the outer and inner cortical surfaces of a frontal lobe colored with their shape indexes. As we can see, most parts of the gyri are automatically identified as ridge, while most parts of the sulci are identified as rut, which coincides with our knowledge of the cortical structure.

D. Regional Cortical Thickness

We further applied our algorithm to seven high-resolution MRI data sets (SPGR, 2NEX, $1.2 \times 1.2 \times 1.2$ mm³ voxels) of normal males (average IQ = 109) to study the pattern of regional cortical thickness.

The lobes of the brain were labeled using locally developed software [29] in conjunction with the ANALYZE software package [30]. The frontal lobe was segmented by tracing the central sulci directly on 3-D renderings of the brain and then in successive 2-D slices extending the traces to the depth of the sulci and through the white matter to the midline at an angle perpendicular to the interhemispheric fissure. Next, the temporal lobes were segmented by tracing the sylvian fissure on 3-D renderings until the point where the fissure arched upward into the parietal lobe. At that point of inflection, a plane parallel to the AC-PC was used to segment the temporal and parietal lobes. The occipital-parietal boundary was set at midline by placing an oblique plane through the parietoccipital sulcus and a coronal plane at the intersection of the parietoccipital sulcus and the calcarine fissure. Fig. 12 (top) shows the parcellation of the lobes of a cerebrum, as described above.

Shown in Fig. 12 (bottom) are the top and back views of an outer cortical surface colored with cortical thickness. Table III lists the cortical thickness measurements in four lobes over the seven subjects. We compared the mean thickness of each lobe to the data on 63 males from the postmortem study by Pakkenberg and Gundersen [27], and found the exact same rank ordering of thickness; the frontal cortex was the thickest and the occipital the thinnest. The postmortem data measurements were 5–14% thinner by lobe than our *in*

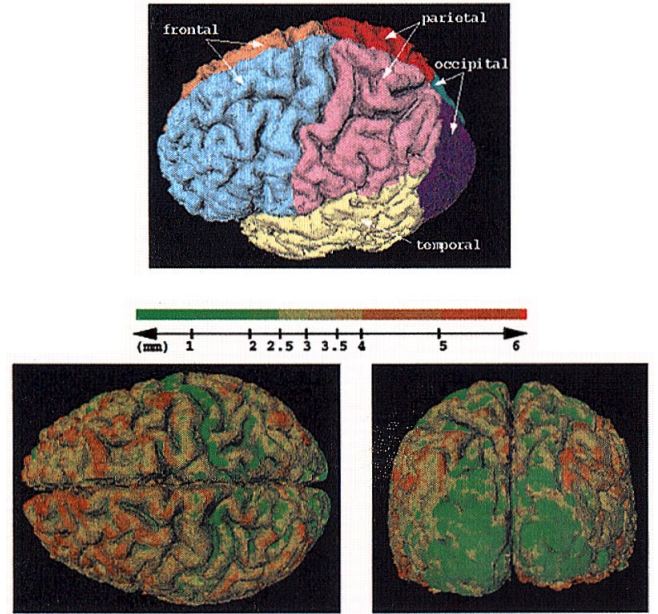


Fig. 12. Regional cortical thickness. (Top) Parcellation of lobes where regional cortical thickness is measured. (Bottom) Top and back views of an outer cortical surface colored with cortical thickness.

TABLE III
REGIONAL CORTICAL THICKNESS (IN mm) OF SEVEN NORMAL MALE SUBJECTS

frontal	temporal	parietal	occipital
3.35	3.18	2.81	2.82
3.47	3.14	2.95	2.95
3.18	3.00	2.70	2.67
3.18	2.83	2.59	2.46
3.39	3.30	2.95	2.60
2.97	2.95	2.56	2.44
2.99	3.04	2.78	2.44

vivo data. This might be due to both the older age of the subjects, tissue shrinkage in the postmortem study, and volume averaging with our MRI data. However, it is important to note that the variability of thickness was the same for both samples (about 0.15 mm). This gradient of thickness from front to back in the brain is well known and due to the greater number of large pyramidal neurons in the anterior as compared to the posterior cortices.

A repeated measures analysis of variance (ANOVA) tested whether cortical thickness differed by lobe, and found significant differences between the four lobes ($F[3, 27] = 56.3$, $p < .0001$). Post hoc paired t tests showed that the frontal lobe and temporal lobes were each significantly thicker than either the parietal and occipital lobe (p 's $< .001$), but they did not differ in thickness from one another. Likewise, parietal and occipital lobe thickness were not significantly different.

E. User Interaction and Speed Issue

In addition to robustness and accuracy, minimum user interaction and computational efficiency have always been two important issues in the problem of segmenting and measuring the cortex. For an expert to manually isolate the nonbrain

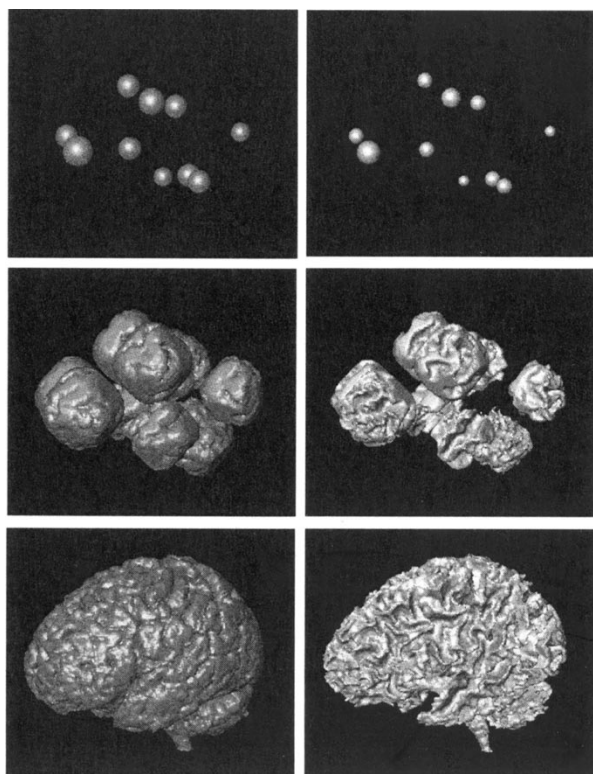


Fig. 13. Coupled-surfaces propagation on the same brain image as in Fig. 7, but with a different set of initializing spheres. For the two final results from different initialization, the TP rate of one with respect to the other is over 99.5%, and the FP rate is less than 0.5%, which demonstrates our algorithm's robustness to initialization.

tissue (using a combination of image thresholding, region growing, and fine editing with manual tracing slice by slice to carefully remove any nonbrain voxels, such as the CSF, within sulci and the dura) alone can take about 2 h. (Structures such as the dura and the CSF in sulci can only be removed by careful slice-by-slice inspection. Therefore, considering the thoroughness and obsessiveness of the fine editing, we believe 2 h is a fair estimate of the processing time). The manual tracing of cortical gray matter is even more time consuming. MacDonald *et al.* deformed two ellipsoids with intersurface constraints to approximate the inner and the outer cortical surfaces. Their processing time for such segmentation on each subject was reported to be 100 h on an SGI Origin 200 R10000 processor running at 180 MHz [22]. In [5], it was reported that the ribbon algorithm was a fairly computationally demanding iterative procedure, while manual placement of the initial cortical surface and a multiscale formulation could decrease the computational load. The processing time per subject for Xu's method was reported to vary between 4.5 to 6.5 h on an SGI O2 workstation with a 174-MHz R10000 processor [41].

The initialization for our algorithm only requires the user to specify several pairs of concentric spheres in the unedited images, which can be done with several mouse clicks within seconds. It should be emphasized that neither the number nor the placement of the spheres (within a broad range of acceptable values) affects the accuracy or the reproducibility of the final result. To illustrate this, Fig. 13 shows the coupled-surfaces propagation on the same brain, as in Fig. 7, but from

a different set of initializing spheres. The final results of the surfaces show little visual difference. Quantitatively, the TP rate of one with respect to the other is over 99.5% and the FP rate is less than 0.5%.

For a 3-D image ($1.2 \times 1.2 \times 1.2 \text{ mm}^3$ in voxel size) of the whole brain, our algorithm runs in about 1 h on a SGI Indigo2 machine with a 195-MHz R10000 processor. Skull-stripping, segmentation and measurement of the cortex are done simultaneously. Comparatively, to our knowledge our algorithm outperforms other related techniques with respect to user interaction and computational efficiency.

IV. SUMMARY AND FUTURE DIRECTIONS

In this paper, we presented a new approach to the segmentation and measurement of cortical structure which is of great interest in the study of the structural and functional characteristics of the brain. Motivated by the fact that the cortex has a nearly constant thickness, we model the cortex as a volumetric layer which is completely defined by the two bounding surfaces and the homogeneity in between. Starting from easily initialized concentric spheres and driven by image-derived information, two interfaces evolve out to capture the inner and outer cortical boundaries, thereby segmenting out the cortical gray matter from the white matter, as well as isolating the brain tissue from the nonbrain tissue. Cortical gray-matter volume and cortical surface area (both inner and outer) are then measured. Due to the coupled level set implementation, the cortical surface curvature and cortical thickness map are also easily obtained. As seen from various experiments, our algorithm is automatic, accurate, robust, and relatively computationally efficient.

We would like to mention that this segmentation method using coupled-surfaces propagation has potential applications in other medical image analysis domains, where a volumetric layer is the study of interest. Examples include the left ventricular (LV) myocardium of the heart and the bounding wall of the liver. Different coupling may be used to tailor the algorithm for specific applications. For example, the endocardial and epicardial walls which bound the thick LV myocardium are loosely coupled instead of tightly coupled, as are the cortical surfaces.

Future directions for this work include the following: finer design of the local feature operator to better model the volume averaging effect; better capturing the homogeneity of the volume; volume measurement on the subvoxel level; possible use of a vector image data set; and testing on image data of abnormal brains.

ACKNOWLEDGMENT

The authors would like to thank J. Rambo and L. Win for their help with the visualization and manual tracing of the MR data. Thanks also go to the McConnell Brain Imaging Center at the Montreal Neurological Institute and the Center for Morphometric Analysis at Massachusetts General Hospital for providing data. Finally, the authors thank the editors and reviewers for a number of suggestions that helped to make this a better paper.

REFERENCES

- [1] S. M. Blinkov and I. I. Glezer, *The Human Brain In Figures and Tables, A Quantitative Handbook*. New York: Plenum, 1968, ch. 10, p. 182.
- [2] H. E. Cline, W. E. Lorensen, R. Kikinis, and F. Jolesz, "Three-dimensional segmentation of MR images of the head using probability and connectivity," *J. Comp. Assisted Tomogr.*, vol. 14, pp. 1037–1045, 1990.
- [3] L. D. Cohen and I. Cohen, "Finite-element methods for active contour models and balloons for 2-D and 3-D images," *IEEE Trans. Pattern Pattern Anal. Machine Intell.*, vol. 15, pp. 1131–1147, Nov. 1993.
- [4] C. A. Davatzikos and J. Prince, "An active contour model for mapping the cortex," *IEEE Trans. Med. Imag.*, vol. 14, pp. 65–80, Mar. 1995.
- [5] C. Davatzikos and R. N. Bryan, "Using a deformable surface model to obtain a shape representation of cortex," *IEEE Trans. Med. Imag.*, vol. 15, pp. 785–795, Dec. 1996.
- [6] A. M. Dale, B. Fischl, and M. I. Sereno, "Cortical surface-based analysis," *NeuroImage*, vol. 9, pp. 179–194, 1999.
- [7] M. P. DoCarmo, *Differential Geometry of Curves and Surfaces*. Englewood Cliffs, NJ: Prentice-Hall, 1976.
- [8] P. A. Filipek, D. N. Kennedy, and V. S. Caviness, "Volumetric analysis of central nervous system neoplasm based on MRI," *Pediatric Neurol.*, vol. 7, pp. 347–351, 1991.
- [9] P. A. Filipek, C. Richelme, D. N. Kennedy, and V. S. Caviness, "The young adult human brain: An MRI-based morphometric analysis," *Cerebral Cortex*, vol. 4, no. 4, pp. 344–360, 1994.
- [10] D. Geman and S. Geman, "Stochastic relaxation, Gibbs distribution and Bayesian restoration of images," *IEEE Trans. Pattern Pattern Anal. Machine Intell.*, vol. 6, pp. 721–741, Nov. 1984.
- [11] "Internet Brain Segmentation Repository (IBSR)," Center for Morphometric Analysis (CMA). Available: <http://neuro-www.mgh.harvard.edu/cma/ibsr>. <http://www.bic.mni.mcgill.ca/>.
- [12] "BrainWeb," McConnell Brain Imaging Center, Montreal Neurological Institute. Available: <http://www.bic.mni.mcgill.ca/>.
- [13] M. Kass, A. Witkin, and D. Terzopoulos, "Snakes: active contour models," *Int. J. Comp. Vision*, vol. 1, pp. 312–331, 1988.
- [14] D. N. Kennedy, P. A. Filipek, and V. S. Caviness, "Anatomic segmentation and volumetric calculations in nuclear Magnetic Resonance imaging," *IEEE Trans. Med. Imag.*, vol. 8, pp. 1–7, 1989.
- [15] J. J. Koenderink and A. J. van Doorn, "Surface shape and curvature scale," *ImageVision Comp.*, vol. 10, pp. 557–565, 1992.
- [16] R. K.-S. Kwan, A. C. Evans, and G. B. Pike, "An extensible MRI simulator for post-processing evaluation," in *Visualization in Biomedical Computing (VBC'96)* (Lecture Notes in Computer Science). Berlin, Germany: Springer-Verlag, 1996, vol. 1131, pp. 135–140.
- [17] S. Lakshmanan and H. Derin, "Simultaneous parameter estimation and segmentation of Gibbs random fields using simulated annealing," *IEEE Trans. Pattern Pattern Anal. Machine Intell.*, vol. 11, pp. 799–810, Aug. 1989.
- [18] R. Leahy, T. Hebert, and R. Lee, "Applications of Markov Random Fields in medical imaging," *Information Processing in Medical Imaging*. New York: Wiley-Liss, 1991, pp. 1–14.
- [19] Z. Liang, R. F. Jaszczak, and R. E. Coleman, "Parameter estimation of finite mixtures using the EM algorithm and Information criteria with application to medical image processing," *IEEE Trans. Nucl. Sci.*, vol. 39, pp. 1126–1133, 1992.
- [20] W. Lorensen and H. Cline, "Mar.ing cubes: A high resolution 3D surface construction algorithm," *Comp. Graph. (Proc. SIGGRAPH)*, vol. 21, pp. 163–169, July, 1987.
- [21] D. MacDonald, D. Avis, and A. E. Evans, "Multiple surface identification and matching in Magnetic Resonance images," *Proc. SPIE*, vol. 2359, pp. 160–169, 1994.
- [22] ———, "Proximity constraints in deformable models for cortical surface identification," in *Proc. First Int. Conf. Medical Image Computing Computer-Assisted Intervention*, Boston, MA, 1998, pp. 650–659.
- [23] R. Malladi, J. A. Sethian, and B. C. Vemuri, "Shape modeling with front propagation: A level set approach," *IEEE Trans. Pattern Pattern Anal. Machine Intell.*, vol. 17, pp. 158–174, Feb. 1995.
- [24] R. Malladi, R. Kimmel, D. Adalsteinsson, G. Sapiro, V. Caselles, and J. A. Sethian, "A geometric approach to segmentation and analysis of 3D medical images," in *Proc. MMBIA*, 1996.
- [25] R. Malladi and J. A. Sethian, "A real-time algorithm for medical shape recovery," in *Proc. Int. Conf. Computer Vision*, 1998, pp. 304–310.
- [26] J. C. Rajapakse and F. Fruggel, "Segmentation of MR images with intensity inhomogeneities," *Image Vision Comput.*, vol. 16, no. 3, pp. 165–180, Mar. 1998.
- [27] B. Pakkenberg and H. J. Gundersen, "Neocortical neuron number in humans: Effect of sex and age," *J. Comparative Neurol.*, vol. 384, pp. 312–320, 1997.
- [28] J. V. Rambo, X. Zeng, R. T. Schultz, L. Win, L. H. Staib, and J. S. Duncan, "Platform for visualization and measurement of gray matter volume and surface area within discrete cortical regions from MR images," in *Proc. 4th Int. Conf. Functional Mapping Human Brain*, 1998, p. 795.
- [29] J. V. Rambo, R. T. Schultz, L. H. Staib, L. Win, X. Zeng, J. S. Duncan, "Fast interactive volumetric segmentation of MR brain images," *NeuroImage*, submitted for publication.
- [30] R. A. Robb, Analyze software, Biomedical Imaging Resource, Mayo Foundation/Clinic, Rochester, MN, 1990.
- [31] R. T. Schultz and A. Chakraborty, "Magnetic resonance image analysis," in *Handbook of Human Brain Function: Neuroimaging*, E. Bigler, Ed. New York: Plenum, 1996, pp. 9–51.
- [32] L. D. Selemon, G. Rajkowska, and P. S. Goldman-Rakic, "Abnormally high neuronal density in the schizophrenic cortex, a morphometric analysis of Prefrontal Area 9 and Occipital Area 17," *Arch. Gen. Psychiatry*, vol. 52, pp. 805–828, 1995.
- [33] J. A. Sethian, *Level Set Methods: Evolving Interfaces in Geometry, Fluid Mechanics, Computer Vision and Materials Science*. New York: Cambridge Univ. Press, 1996.
- [34] K. Siddiqui, Y. Berube, A. Tannenbaum, and S. W. Zucker, "Area and length minimizing flows for shape segmentation," *IEEE Trans. Image Processing*, vol. 7, no. 3, pp. 433–443, 1998.
- [35] L. H. Staib and J. S. Duncan, "Model-based deformable surface finding for medical images," *IEEE Trans. Med. Imag.*, vol. 16, pp. 720–731, 1996.
- [36] L. H. Staib, A. Chakraborty, and J. S. Duncan, "An integrated approach for locating neuroanatomical structure from MRI," *Int. J. Patt. Recognit. Art. Intell. (Special Issue on MR Brain Image Analysis)*, vol. 11, pp. 1247–1269, 1997.
- [37] J. Talairach and P. Tournoux, *Co-planar Stereotaxic Atlas of the Human Brain*. New York: Thieme, 1988.
- [38] P. C. Teo, G. Sapiro, and B. A. Wandell, "Creating connected representations of cortical gray matter for functional MRI visualization," *IEEE Trans. Med. Imag.*, vol. 16, pp. 852–863, 1997.
- [39] K. L. Vincken, A. Koster, and M. A. Viergever, "Probabilistic hyperstack segmentation of MR brain data," in *Proc. 1st Int. Conf. Computer Vision, Virtual Reality Robotics Medicine*, Nice, France, 1995, pp. 351–357.
- [40] W. M. Wells, W. Grimson, R. Kikinis, and F. A. Jolesz, "Adaptive segmentation of MRI data," *IEEE Trans. Med. Imag.*, vol. 15, pp. 429–442, Aug. 1996.
- [41] C. Xu, D. L. Pham, J. L. Prince, M. E. Etemad, and D. N. Yu, "Reconstruction of the central layer of the human cerebral cortex from MR images," in *Proc. First Int. Conf. Medical Image Computing and Computer-Assisted Intervention*, Boston, MA, 1998, pp. 481–488.
- [42] X. Zeng, L. H. Staib, R. T. Schultz, and J. S. Duncan, "Volumetric layer segmentation using coupled surfaces propagation," in *Proc. IEEE Conf. Computer Vision and Pattern Recognition*, Santa Barbara, CA, 1998, pp. 708–715.